Tornadogenesis with and without a Dynamic Pipe Effect

R. JEFFREY TRAPP AND ROBERT DAVIES-JONES

National Severe Storms Laboratory, NOAA, Norman, Oklahoma

(Manuscript received 7 February 1996, in final form 20 June 1996)

ABSTRACT

A dynamic pipe effect (DPE) has been used previously to explain the descent from aloft of tornadic vortex signatures (TVSs), and presumably embryonic tornadoes, prior to the near-ground spinup of the tornado. But for many tornadoes the TVS appears to form simultaneously over a depth spanning the lowest few kilometers. A numerical model is used to determine the conditions under which a tornado is or is not preceded by a DPE. The model governs two-dimensional, axisymmetric, forced convection inside a closed, impermeable cylinder that rotates at a constant rate. Motion relative to the tank is initiated by a time-independent buoyancy field that is varied in a suite of experiments. The need for a DPE in vortex development in the model is shown to depend on trajectories of high-angular-momentum air, driven at least initially by this buoyancy field. Indeed, when buoyancy is confined primarily to midlevels, convergence at the foot of the vertical axis is weak initially, parcels with high angular momentum approach closest to the axis first at midlevels, and the vortex forms aloft (mode I). As the vortex intensifies and becomes cyclostrophically balanced, its central pressure drops and lateral motion into its core is inhibited. The resultant vertical pressure gradient and radial convergence below the vortex core increase, allowing parcels to approach the axis—and thus affording vortex spinup—at progressively lower levels. This process is the DPE. When significant buoyancy is present at low levels, air parcels that nearly conserve angular momentum are transported close to the axis over a relatively deep layer inclusive of the lower levels. The vortex in this case forms at low and midlevels at the same time, precluding a need for a DPE (mode II).

A simple analytical model is used to illustrate the two modes of vortex formation, and to generalize the conclusions drawn from the numerical model. A time-dependent version of the Burgers–Rott vortex due to Rott demonstrates vortex formation without a DPE. In this exact solution of the Navier–Stokes equations, horizontal convergence and angular momentum are independent of height, and the meridional flow is steady. A simple analytical solution for the DPE has not been found. However, it can be shown qualitatively that a vortex that develops aloft, because either the large-scale convergence or the ambient angular momentum increases with height, induces below itself an axial jet and increased radial inflow at low levels.

1. Introduction

The successful tornadogenesis paradigm must explain why tornadic vortex signatures (TVSs) and embryonic tornadoes are sometimes, but not always, observed aloft prior to tornadogenesis. A TVS is a large value (typically $>1 \times 10^{-2}$ s^{-1}) of azimuthal shear between two adjacent sampling volumes in a Doppler-radar radial-velocity field and usually forms within (but not necessarily in the center of) a mesocyclone (e.g., Brown et al. 1978). It is presumed that a TVS is a degraded image of an embryonic or actual tornado. According to Davies-Jones (1986), nearly all TVSs are associated with tornadoes, though not all tornadoes have a detectable TVS because of radar sampling limitations (e.g., the tornado may be too small and/or too far from the radar). In the events studied by Brown et al. (1978), the TVS typically formed at middle levels, built both upward and downward in time, reached very low levels coincident with tornado ''touchdown,'' intensified as the tornado grew larger, and ultimately weakened and disappeared at all levels as the tornado decayed. As analyzed by Vasiloff (1993) and later simulated by Trapp (1994) and Trapp and Fiedler (1995), TVSs may also form and later intensify near the ground or over a large depth inclusive of the ground. Based on the recent study by Trapp and Mitchell (1995), this may be the mode of development in as many as 50% of all TVSs. The embryonic tornado circulation in these cases is probably not detectable on radar until a few minutes prior to tornado formation; in contrast, the archetypal TVSs in Brown et al. precede tornado touchdown by a few *tens* of minutes.

The relevance and ''dynamical connection'' of a TVS aloft with tornadogenesis has been questioned (Rotunno 1986). Indeed, the notion that an incipient tornado develops aloft and gradually descends to the ground is counter to thoughts that the tornado develops near the ground once strong radial convergence within the turbulent boundary layer rapidly amplifies vorticity asso-

Corresponding author address: Dr. R. Jeffrey Trapp, National Severe Storms Laboratory, 1313 Halley Circle, Norman, OK 73069.
E-mail: trapp@nssl.uoknor.edu

ciated with the low-level mesocyclone (Rotunno 1986; Rasmussen et al. 1994).

The ''dynamic pipe effect'' (hereinafter DPE) has been offered as an explanation for the descent of the TVS and the final spinup of the tornado (Leslie 1971). A vortex in cyclostrophic balance at some height permits little to no radial flow into its core because the radial pressure gradient force is in stable equilibrium with the centrifugal force, but allows upward (downward) accelerations from below (above) its core by the rotationally induced, vertical pressure-gradient force (VPGF). Morton (1966) demonstrated that the flow in a tornado-like vortex is in cyclostrophic balance, and, as described by Leslie (1971), Smith and Leslie (1979), and others, such a vortex that forms aloft acts essentially as a pipe, ''drawing air toward its lower end.'' The radial convergence associated with the inflow into the lower end of the ''pipe'' concentrates ambient vertical vorticity, ultimately establishing a new level of cyclostrophic balance. This process then repeats itself at progressively lower heights until the vortex extends to the ground [provided there is ambient vertical vorticity sufficiently close to the ground; Smith and Leslie, (1978)]. Note that while the downward progression takes place, the vortex also builds upward through advection of vorticity. Note also that ''ambient vertical vorticity'' refers here to that which precedes the tornado in the final stage of its genesis and is present around the tornado on the mesocyclone scale; the ''mesocyclone'' itself typically originates from horizontal vorticity. Smith and Leslie (1979) claim that their description (and simulation) of tornado descent to the ground is consistent with the TVS evolution observed in the Union City tornadic thunderstorm (see Brown et al. 1978). Wicker and Wilhelmson (1995) argue, in a similar vein but on a larger scale, that an increase in rotation aloft within the mesocyclone causes an upward-directed VPGF, and then an ''updraft pulse,'' that concentrates subcloud vertical vorticity into a tornado.

In this context, the DPE should not be mistaken with the effects of an endwall boundary layer on a vortex. It is well known that the cyclostrophic balance of a vortex is upset in the boundary layer's inner or surface layer because friction reduces the tangential wind and centrifugal force to zero at the ground but the inward radial pressure-gradient force does not vanish there. Strong inflow within the surface layer, driven by the unbalanced inward pressure gradient force, transports fluid parcels closer to the axis than would have otherwise been possible without friction. Subsequent mass and angular momentum transport proceeds radially inward to a radius on the order of the surface-layer depth, whereupon the flow turns vertical (Wilson and Rotunno 1986). This region is termed the ''corner'' region (see Snow 1982), in which the swirling surface layer may ''erupt'' into an intense axial jet (Burgraff et al. 1971). The frictionally induced flow comprises a *secondary* circulation within the *primary* radial–vertical (or meridional) circulation induced by the buoyancy forcing aloft. This secondary circulation significantly increases windspeeds in endwall vortices and tornadoes (Fiedler and Rotunno 1986).

We begin this investigation of tornadogenesis and the DPE by assuming that most of the disparate TVS (and presumably tornado/embryonic tornado) observations are the result of physical differences rather than an artifice of radar sampling (see Wood and Brown 1992), while accepting that some observations may very well be attributable to radar sampling inadequacies. As an example, we cannot rule out that the apparent lack of a DPE is in fact an uncharacteristically fast DPE that occurs between radar volume scans (i.e., within $\sim$5 min). Nowhere in the literature is there a suitable explanation of the observed dichotomy of TVS development and thus of tornadogenesis modes. The research presented herein is aimed specifically at determining the conditions for both presence and absence of a DPE. In the numerical models of Leslie (1971), Leslie and Smith (1978), and Smith and Leslie (1978, 1979), the upward body or buoyancy force is located at mid- to upper levels, and the vortex always formed aloft. Thus, our starting point and initial hypothesis is that DPE presence depends on properties of the primary meridional circulation driven by the parent thunderstorm.

In section 2, we describe the numerical model used to simulate the genesis of tornado-like vortices within a rotating updraft. When buoyant convection within the model domain is varied in a suite of experiments described in section 3, we indeed find instances in which a DPE is required in the vertical formation of a vortex, and others when it is not. An analytical model that illustrates the two types of genesis is presented in section 4. Finally, in section 5 we discuss, in the light of our results, the genesis of different types of tornado and other convective vortices.

2. Description of the model

The model governs two-dimensional (2D), axisymmetric forced convection inside a closed, impermeable cylinder that rotates at a constant rate Ω. Physically, this can be viewed as a rotating updraft that draws upon ''ambient'' vertical vorticity of 2Ω, within which tornadogenesis occurs. Motion relative to the rotating tank is initiated from a quiescent state by a body force, $b(r, z)$, which we also refer to as buoyancy, that is most intense on the symmetry axis. We use this particular modeling approach because we require explicit control of the shape, position in the domain, and magnitude of the updraft forcing. The model is made dimensionless by a convective velocity scale W (defined by the vertical integral of the buoyancy; see below) and by the depth of the model domain H (nominally, the depth of the storm). The character of the flow is thus dependent on the nondimensional eddy viscosity, buoyancy, angular velocity, and aspect ratio of the cylinder, as well as on

the choice of initial and boundary conditions. Our hypothesis rests on those parameters that most strongly influence the primary meridional circulation, namely Ω and those that define b. Although discussed in the context of vortex intensity rather than vortex development, Fiedler (1994) found little sensitivity of simulated vortices to the nondimensional radius R of the outer wall (and implicitly to the aspect ratio) provided that R $\geq$ 2. Fiedler also determined from his simulations that "the maximum steady-state windspeed is largely independent of Reynolds number when the ambient angular momentum is sufficiently large."

The governing equations in cylindrical coordinates (r, θ, z) are

$$\frac{du}{dt} - \frac{v^2}{r} - 2\Omega v = -\frac{\partial \phi}{\partial r} + \nu\left(\nabla^2 u - \frac{u}{r^2}\right), \quad (1)$$

$$\frac{dv}{dt} + \frac{uv}{r} + 2\Omega u = \nu\left(\nabla^2 v - \frac{v}{r^2}\right), \quad (2)$$

$$\frac{dw}{dt} = -\frac{\partial \phi}{\partial z} + b + \nu\nabla^2 w, \quad (3)$$

and

$$\frac{\partial ru}{\partial r} + \frac{\partial rw}{\partial z} = 0, \quad (4)$$

where (u, v, w) is velocity, $d/dt = \partial/\partial t + u\partial/\partial r + w\partial/\partial z$, ϕ is a pressure-like variable $(= p/\rho - \Omega^2 r^2/2)$, b is the time-independent buoyancy, and ν is the inverse Reynolds number (hereinafter referred to as eddy viscosity and assigned a value of 0.0005). Details concerning the numerical approximations to these equations can be found in Fiedler (1994).

Buoyancy is defined as

$$b(r, z) = \begin{cases} \dfrac{\pi}{8h} \cos\left(\dfrac{\pi s}{2h}\right), & s \leq h, \\ 0, & s \geq h, \end{cases} \quad (5)$$

where

$$\frac{s^2}{h^2} \equiv \frac{r^2}{r_0^2} + \frac{(z - z_0)^2}{h^2}.$$

Thus, h $(\leq z_0 \leq 1/2)$ and r_0 $(\leq 1/2)$ are the semiheight and radius, respectively, of the fixed ellipsoidal "bubble," which is centered at $r = 0$, $z = z_0$. The vertical integral

$$\int_{z=z_0-h}^{z=z_0+h} b(0, z')\, dz' = \frac{1}{2} \quad (6)$$

defines the convective available potential energy (CAPE) on the central axis, which also defines a theoretical bound (viz., the "thermodynamic speed limit") on the updraft speed of $W = \sqrt{2\text{CAPE}} = 1$ and on the azimuthal wind speed of $V = \sqrt{\text{CAPE}} = 1/\sqrt{2}$ (e.g., Fiedler 1994).

TABLE 1. Description of model experiments. In the case names, the leading F or N denotes free-slip or no-slip lower boundary condition, and the R or N in the fourth place signifies rotation ($\Omega = 0.1$) or no rotation, respectively. An appended "L" (in the fifth place) denotes a lower center of the bubble ($z_0 = 1/4$ instead of 1/2). The first digit is the domain depth/bubble depth, $1/2h$), and the second digit is the domain depth/bubble diameter, $(1/2r)$. For example, the first digit is 1 when the bubble is as deep as the domain ($2h = 1$), and 2 when it is half as deep ($2h = 1/2$).

Case	h	z_0	r_0	Ω	Boundary condition	DPE?
F11N	1/2	1/2	1/2	0	free slip	
N11N	1/2	1/2	1/2	0	no slip	
F11R	1/2	1/2	1/2	0.1	free slip	no
N11R	1/2	1/2	1/2	0.1	no slip	no
F22N	1/4	1/2	1/4	0	free slip	
F22NL	1/4	1/4	1/4	0	free slip	
N22N	1/4	1/2	1/4	0	no slip	
F22R	1/4	1/2	1/4	0.1	free slip	yes
F22RL	1/4	1/4	1/4	0.1	free slip	no
N22R	1/4	1/2	1/4	0.1	no slip	yes
F44R	1/8	1/2	1/8	0.1	free slip	yes
N44R	1/8	1/2	1/8	0.1	no slip	yes
F21R	1/4	1/2	1/2	0.1	free slip	yes
F12R	1/2	1/2	1/4	0.1	free slip	no
F41R	1/8	1/2	1/2	0.1	free slip	yes
F14R	1/2	1/2	1/8	0.1	free slip	no

The upper boundary ($z = 1$) and outer wall ($r = 2$) are considered rigid, impermeable, and no slip; the central axis ($r = 0$) is a symmetry axis; and the lower boundary ($z = 0$) can be made either free slip or no slip. The grid, consisting of 61 points in both the radial and vertical directions, is stretched according to the functions described in Fiedler (1995) and provides high resolution in the vicinity of the central axis and viscous boundary layer.

3. Results

Experimentation with this model is designed to test the aforementioned hypothesis and will thereby consist of a series of integrations in which the buoyancy distribution is varied in both the radial and vertical directions by varying h, r_0, and z_0 in Eq. (5). For future reference, details of the experiments are provided in Table 1. Before proceeding, it is necessary to determine approximately the optimal matching, in terms of an intense steady-state vortex, of Ω and a given buoyancy field (Smith and Leslie 1978). Once found, this value of Ω will be used in the subsequent experiments.

a. The steady-state vortex and choice of rotation rate

Davies-Jones (1973) summarizes the change in vortex flow structure as the rotation rate is altered. Consider model integrations in which the lower boundary is free slip and $b(r, z)$ is defined with $h = r_0 = ½$. Consistent with Davies-Jones's discussion we find that for large rotation rates (say, $\Omega \geq 2$) the solution rapidly evolves

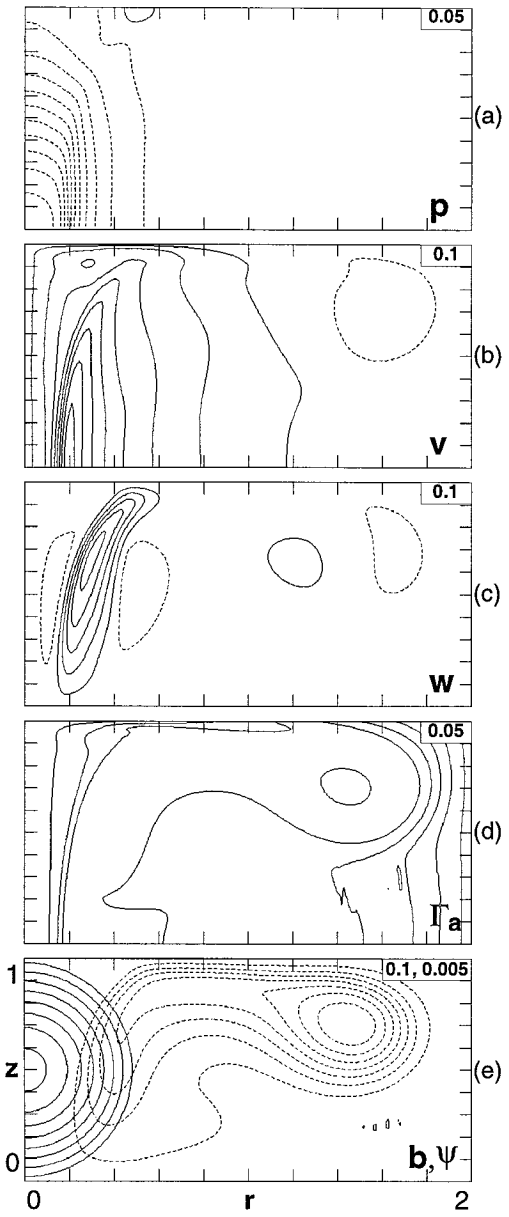

FIG. 1. Contours of (a) pressure, (b) tangential velocity, (c) vertical velocity, (d) absolute angular momentum, and (e) streamfunction and buoyancy for the steady-state solution of experiment F11R. In this contour plot and all that follow, the contour intervals are indicated in the top right-hand corner of each plot, contour values begin at one-half the contour interval, and solid (dashed) contours indicate positive (negative) values for all fields except streamfunction, for which the opposite sign convention applies.

into one of a broad vortex of rather shallow depth, in a meridional circulation that consists of two concentric cells with downflow along the axis and outer rim and updraft along the interface between cells; a steady state is never reached. A very small rotation rate of $\Omega = 0.002$ results in a single meridional circulation cell with a weak, narrow vortex. The optimal matching of buoyancy (again, with $h = r_0 = ½$; see Fig. 1e) and rotation appears to occur when $\Omega = 0.1$. This is confirmed by the two-celled steady-state vortex solution for FllR shown in Fig. 1. The extrema, $p_{\min} = -0.56$, $v_{\max} = 0.80$, and $w_{\max} = 0.49$ are close to their theoretical bounds (Fiedler 1993).

The optimum matching between buoyancy and rotation at $\Omega = 0.1$ can be explained as follows. First, note that the equation set (1)–(4) has a steady, inviscid, hydrostatic, and gradient-flow solution given by

$$\left.\begin{aligned} \phi(r, z) &= -\int_z^1 b(r, z')\, dz', \\ v(r, z) &= \sqrt{r\frac{\partial \phi}{\partial z} + \Omega^2 r^2} - \Omega r, \\ u &= w = 0; \end{aligned}\right\} \tag{7}$$

(see Fiedler 1993, his Fig. 7). In this solution, the meridional flow is completely choked, the maximum tangential velocity is located at the lower surface, and solid-body rotation prevails outside $r = r_0$. The steady-state solutions in the experiments with rotation and a free-slip lower surface are two-celled vortices embedded in weak meridional circulation [as depicted in Fig. 1e by the Stokes streamfunction ψ, defined by $u \equiv -(1/r)\partial\psi/\partial z$, $w \equiv (1/r)\partial\psi/\partial r$] and are similar to the balanced vortices given by Eqs. (7) [see Fig. 1 and Fiedler (1993)].

The balanced vortex solution satisfies the azimuthal vorticity equation,

$$\frac{\partial \Gamma_a^2}{\partial z} = r^3 \frac{\partial b}{\partial r}, \tag{8}$$

which represents a balance of torques associated with vertical variation in the centrifugal force and radial gradient in the body force. Here, $\Gamma_a \equiv vr + \Omega r^2$ is the absolute angular momentum, which is conserved following a fluid parcel in the inviscid limit (see Figs. 1d,e). Because the fluid is initially in solid-body rotation with the tank, $\Gamma_a = \Omega Q^2$ in this limit, where Q is the initial radius of a parcel. Integrating (8) with respect to z yields the approximate balance condition $\Omega \sim r_0/\sqrt{2}Q'^2$, where Q' is a representative value of Q in the body-force gradient. We obtain $\Omega \sim 0.1$ for $r_0 = ½$, $Q' \sim R = 2$. If Ω is too small, the balanced solution is unattainable because the flow is dominated by buoyancy; in other words, the centrifugal torque is too small to balance the buoyancy torque. If Ω is too large, the balance is achieved by minor horizontal displacements of parcels ($Q' \ll R$), resulting in a rotation-dominated flow in which there is relatively low amplification of background vertical vorticity in the steady-state vortex.

b. Solutions with zero ambient rotation

Notice that ψ and Γ_a are the primary variables because the boundary conditions and governing equations can be reduced to conditions and two equations in these two

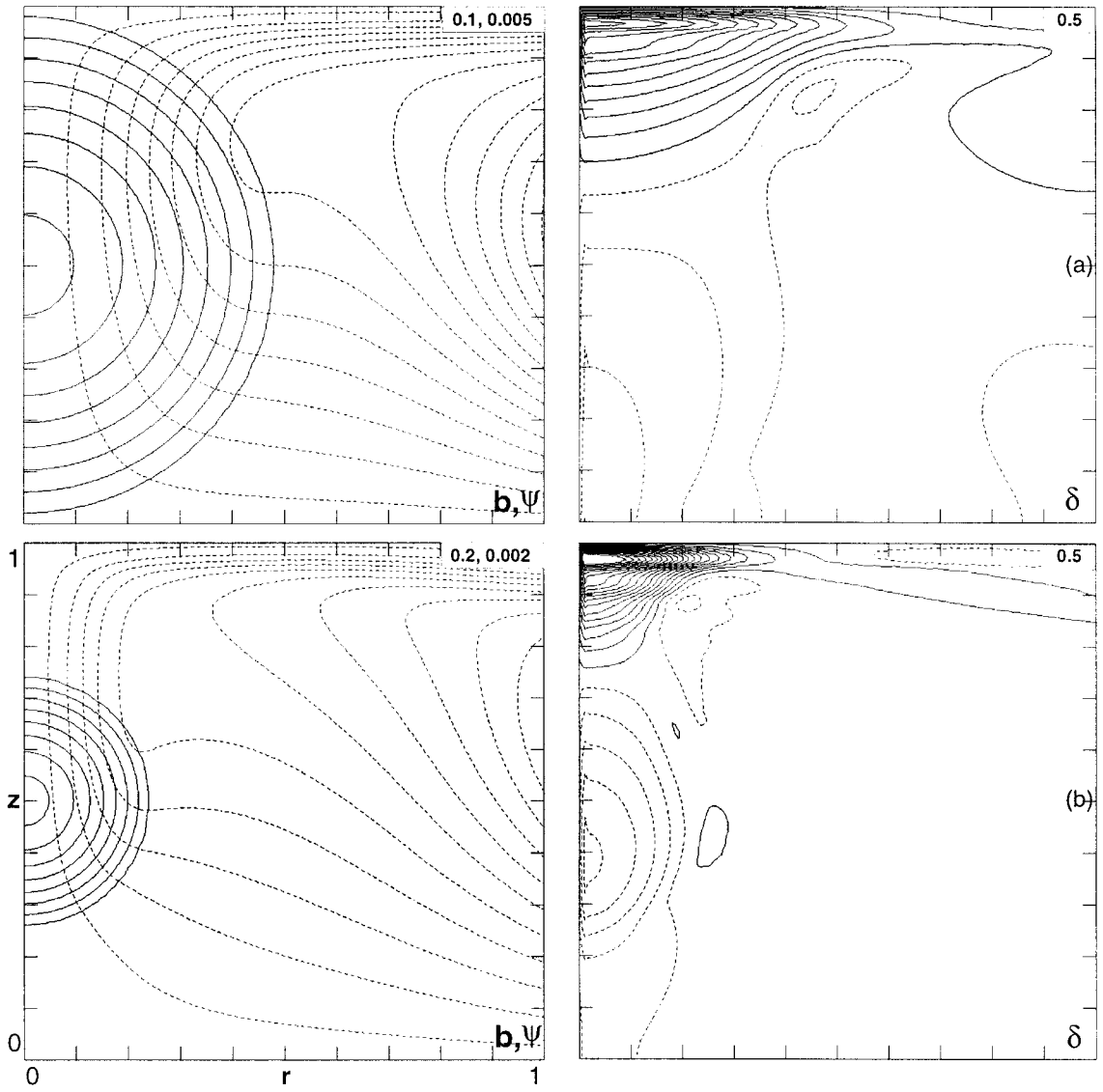

FIG. 2. Contours of streamfunction, buoyancy, and horizontal divergence for the steady-state solution in experiments (a) F11N and (b) F22N. Only a portion ($0 \le r \le 1$, $0 \le z \le 1$) of the domain is shown.

unknowns and because all other quantities can be computed from the solutions for ψ and Γ_a. Using the material near-conservation of Γ_a, one can guess the characteristics of vortex development from knowledge of the parcel trajectories in the corresponding nonrotating case. Hence, we first examine some nonrotating, steady-state solutions.

Plotted in Figs. 2a,b are the buoyancy field and steady-state streamfunction and divergence fields for cases F11N and F22N, in which a free-slip lower boundary condition is imposed, $z_0 = ½$, $\Omega = 0$, and $h = r_0 = ½$ and $h = r_0 = ¼$, respectively (see Table 1). These solutions, wherein $w_{\max} \approx 0.8 < W$ and $w_{\max} \approx 1.0 = W$, respectively, become steady by approximately $t = 40$. Thus, viscosity in the model is large enough to dissipate most of the kinetic energy (KE) of the fluid gained during repeated passes through the body-force region, so that the thermodynamic speed limit is not violated (as it would be in the inviscid limit owing to gains in KE each cycle). Noteworthy is the penetration of flow toward the central axis and significant convergence below $z = 0.2$ in Fig. 2a (and in experiment F22NL; not shown), and the lack of such low-level axial penetration and convergence in Fig. 2b. Nonrotating solutions with no slip at the ground are similar to the corresponding free-slip solutions apart from the added feature of a thin boundary layer.

For the sake of gaining some physical insight into the cases with $\Omega \neq 0$, consider Γ_a to be a passive conservative scalar for the moment. This is equivalent to ne-

glecting the effect of centrifugal forces on the meridional circulation. The buoyancy-forced meridional circulation would transport parcels with high Γ_a to small radii at low levels in F11N and in F22NL, but not in F22N. Thus, we anticipate that modification of the streamfunction field by the swirling flow (via the DPE) is necessary (unnecessary) for near-ground vortexgenesis in F22R (F11R and F22RL), where convergence near the ground is weak (significant) initially.

c. Vortex development without a DPE

We now focus on how vortices develop en route to the steady solution, beginning with experiment F11R, in which $h = r_0 = ½$, $z_0 = ½$, $\Omega = 0.1$, and the lower boundary condition is free slip. Free-slip cases are presented first in order to isolate the DPE from the effects of an endwall boundary layer. Contour plots of tangential velocity, streamfunction, and vertical velocity (Fig. 3) depict vortexgenesis as well as a subsequent evolution toward a two-celled vortex solution (and toward the steady-state solution shown in Fig. 1). Inspection of these plots leads us to propose that a DPE does not play a significant role in the vertical development of the vortex. Indeed, the tangential velocity field in Fig. 3a seems to develop either upward or, at times, uniformly over a broad depth, as expected based on angular momentum transport of parcels by the broad meridional circulation (Fig. 3b). Convergence (the vertical gradient of w) near the axis appears to be fairly uniform from near the ground to midlevels during the initial stages of vortex development (Fig. 3c). The downward-building axial downdraft, forced by an adverse vertical pressure gradient, occurs primarily after the vortex is well established (e.g., by $t = 6$; see Fig. 3c). It is prudent to note that the vortex evolution just described (and also to be described in section 3d) is independent of model initialization—that is, whether the model is initialized with a quiescent state (as in the case presented) or with the steady, meridional flow of the nonrotating companion experiment.

An argument about a DPE based only on these contour plots is admittedly a bit tenuous. More insight regarding the dynamics of the meridional flow can be drawn from an analysis of the forcing terms in the axial momentum equation [Eq. (3)]. As part of this analysis, we follow Schlesinger (1980), Klemp and Rotunno (1983), and others, and decompose the pressure into

$$\phi = \phi_{dn} + \phi_b \tag{9}$$

or, contributions to pressure from dynamic (and viscous) effects (ϕ_{dn}) and from buoyancy (ϕ_b). This is accomplished by taking the divergence of the equation of motion and then using the mass continuity equation [Eq. (4)] to obtain Poisson equations for ϕ_{dn} and ϕ_b (see Klemp and Rotunno 1983, their appendix A). Our approach here is to numerically solve one of the Poisson equations

$$\nabla^2\phi_b = \frac{\partial b}{\partial z} \tag{10}$$

for ϕ_b, using Neumann conditions, $\partial\phi_b/\partial n = \mathbf{n}\cdot(b\mathbf{k})$ (where $\mathbf{n}$ and $\mathbf{k}$ are unit vectors normal to the boundary and in the vertical direction, respectively), at each of the boundaries, and then to determine ϕ_{dn} as a residual from Eq. (9). Note that the ϕ_b field is stationary.

The decomposed vertical pressure-gradient force and buoyancy force are evaluated at $r = 0$ and graphed in Fig. 4 for several times during vortex development in case F11R. If a DPE were occurring, we would expect to find a large upward dynamic pressure-gradient force descending in concert with the lower end of the vortex core or ''pipe.'' Instead, we find in Fig. 4 a preponderance of time-independent ''buoyancy forcing'' F_b ($= -\partial\phi_b/\partial z + b$) and an absence of any marked progression of ''dynamics forcing'' F_{dn} ($= -\partial\phi_{dn}/\partial z$).

In experiment F12R ($h = ½$, $r_0 = ¼$), we investigate the effect of reducing the width of the bubble. A DPE signature is also absent in this case (not shown). Relative to F11R, the vertical flow is confined closer to the axis and the radial inflow is reduced. However, parcels still penetrate the axial region over a large depth, precluding a DPE (as in F11R).

Results of an integration with a no-slip lower boundary (N11R) are presented in Fig. 5. The apparent downward progression of tangential- and vertical-velocity maxima (especially the latter) (Figs. 5a and 5c) beginning at $t \approx 3$ may prompt one to suggest a role of a DPE; further analysis argues that this is in fact not the case. Indeed, in Fig. 5b we find no significant change in the near-axis streamlines from F11R until after $t \approx 5$, and then only within the low levels, where the streamlines bend more abruptly with time as a corner region develops. Profiles of dynamics and buoyancy forcing (Fig. 6) provide the most compelling evidence: dynamics forcing becomes dominant as early as $t = 4$, but again, only within the lowest levels, or just above the boundary layer.[1] This is a reflection of a developing axial jet attendant with an *already rotating* boundary layer. In other words, sufficient tangential velocity for low-level vortexgenesis is already present prior to the *apparent* (in the contour plots) ''vortex descent'' from aloft. The intensifying low-level dynamics forcing evident in Fig. 6 is a secondary effect of strong low-level rotation, not an initiator of it (Morton 1966, 186). However, the interaction of the vortex with the lower surface does modify the flow greatly in the lower part of the vortex core, ultimately resulting in wind speeds in the

[1] Because of the relatively low Reynolds number (compared to atmospheric values) used in the model, the depth of the boundary layer (specifically, the inner or surface layer) may be as much as an order of magnitude too large when scaled to the atmosphere (Fiedler 1994).

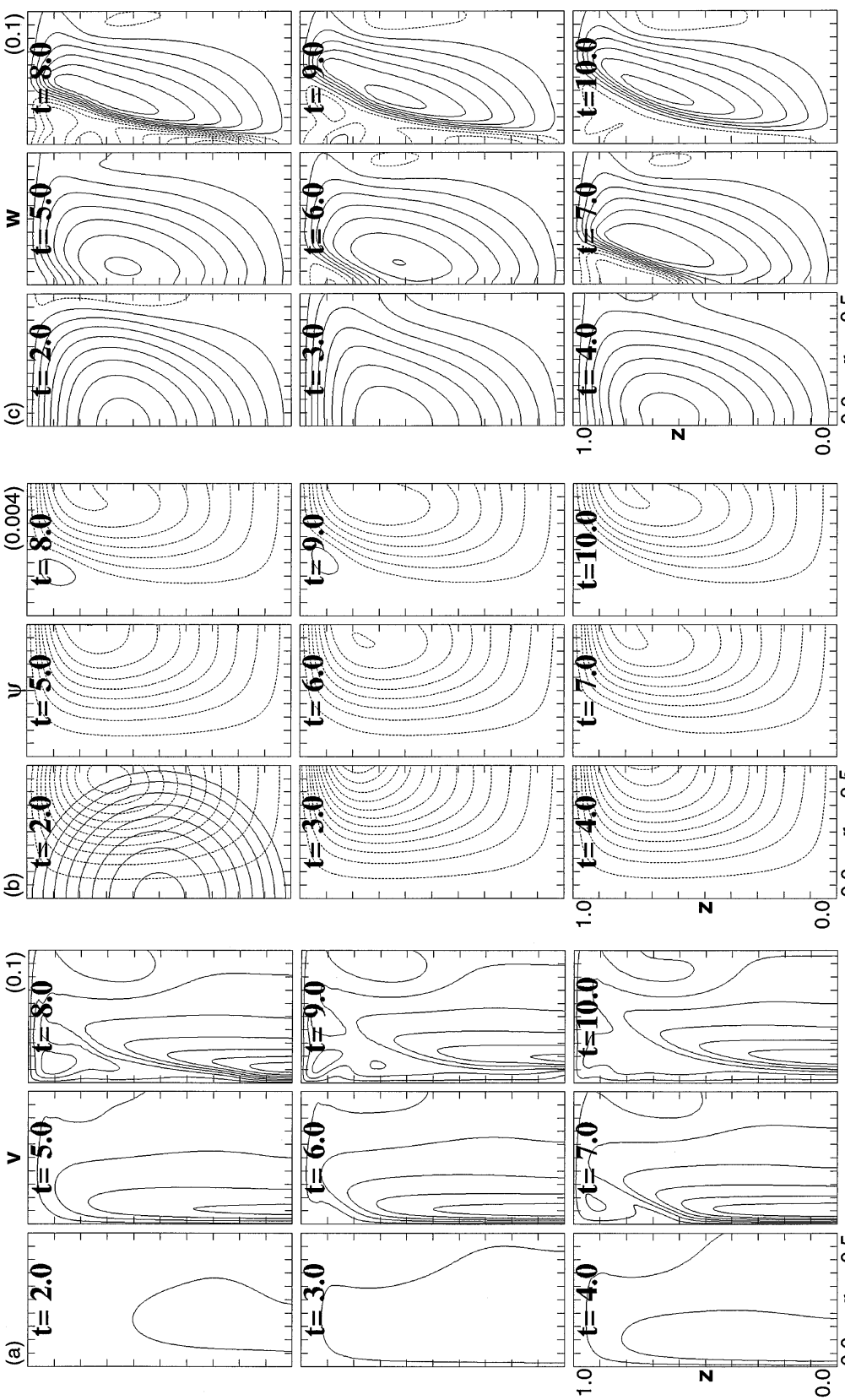

FIG. 3. Contours of (a) tangential velocity, (b) streamfunction, and (c) vertical velocity, at several times during the integration of case F11R. The buoyancy field is displayed in the top left panel in (b). Only a portion ($0 \leq r \leq 0.5$, $0 \leq z \leq 1$) of the domain is shown.

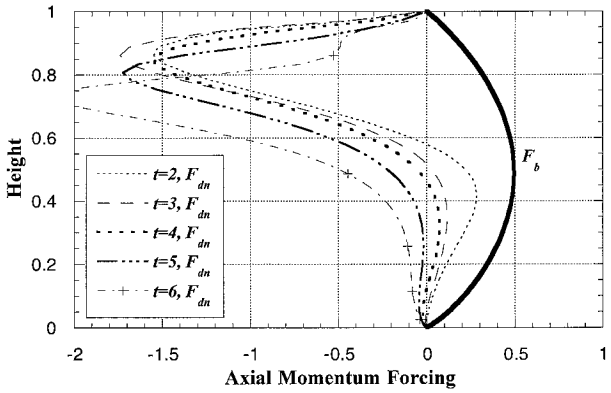

FIG. 4. Axial profiles of "buoyancy forcing" F_b ($= -\partial\phi_b/\partial z + b$), and of "dynamics forcing" F_{dn} ($= -\partial\phi_{dn}/\partial z$) at times $t = 2$, 3, 4, 5, and 6, for case F11R.

endwall vortex that are more intense than any in F11R (see Fiedler and Rotunno 1986).

d. Vortex development with a DPE

We next consider case F22R ($h = r_0 = ¼$, $z_0 = ½$) where the buoyancy field is confined aloft (see Figs. 2b and 7b). The tangential velocity fields during $0 > t \geq 27$ (Fig. 7a) exhibit a maximum that forms and increases at heights $z \geq 0.5$, gradually descends, and then resides at heights $z \leq 0.5$ by $t = 24$; the vortex eventually tends toward the steady vortex solution given in Eq. (7). Concomitant with the descent of the increasing tangential velocity maximum is a subtle increase in the penetration toward the axis of streamlines near $z \approx 0.2$ (Fig. 7b), as well as an increase of radial convergence at progressively lower heights (Fig. 7c). The descent of the intensifying vortex appears to be due to a DPE.

Further evidence is again provided by axial profiles of dynamics and buoyancy forcing (Fig. 8). A remarkable increase and downward progression of the positive dynamics forcing is readily apparent, as is the dominance of dynamics forcing over buoyancy forcing by $t = 21$. Maximum dynamics forcing and maximum vertical acceleration (not shown) lie just below maximum tangential velocity at each time. In our opinion, case F22R exemplifies DPE theory.

A companion no-slip experiment (N22R) has also been performed. Not surprisingly, a DPE appears to operate in this case as well, though with some minor differences. A vortex forms aloft, but intensifies and progresses downward at a slower rate than in F22R (Fig. 9). Consistent with this is the weaker dynamics forcing (Fig. 10) at levels just below the maximum tangential velocity. Vortexgenesis proceeds more slowly than in the free-slip case because parcels that enter the core aloft from low levels (Figs. 9a,b) suffer greater losses of angular momentum through diffusion. Once the boundary layer begins to acquire sufficient rotation through a DPE (as evident in the $t = 15$ profile in Fig. 10), the low-level dynamics forcing increases. The secondary circulation associated with the rotating boundary layer eventually intensifies the near-ground vortex as in case N11R, but at a much later time because of the weaker meridional circulation.

A final experiment (F21R; $h = ¼$, $r_0 = ½$) confirms that presence of a DPE depends on "bubble" depth and not diameter. Indeed, the shallow yet wide buoyancy field in F21R has insignificant buoyancy forcing at low levels, which limits low-level axial penetration, and thus requires a DPE for the downward development of the vortex.

It is instructive at this point to dimensionalize the variables in order to confirm the consistency of the results with atmospheric observations. Suppose the dimensional storm height and CAPE are 12 km and 2500 J kg^{-1}, respectively. The velocity scale is then $W = \sqrt{2 \times 2500} \approx 70$ m s^{-1}, implying a convective timescale of $\approx$3 min. In the absence of a DPE, the near-ground tangential velocity in F11R increases from approximately 10 m s^{-1} (0.15 at $t = 4$) to 30 m s^{-1} (0.45 at $t = 6$) in two time units (see Fig. 3a), or about 6 min. With a DPE, the descent and intensification (from 10 to 30 m s^{-1}) of the vortex in F22R occurs over a period of more than six time units (see Fig. 7a), or about 18 min; both times faithfully represent observed times of tornadic vortex development for the respective modes.

e. Conclusions from numerical experiments

We find that neither presence nor absence of a DPE depends on initialization (whether the rotation precedes the meridional circulation or vice versa), on the nature of the lower boundary (free slip or no slip), or on the radius of the bubble. It does depend on the depth of the bubble when centered at the midlevel.

A DPE seems to be present (absent) whenever the convergence field near the axis is greatest aloft (at the ground). To verify this hypothesis, we ran F22RL, an identical experiment to F22R except that the center of the bubble (z_0) is lowered from $z = ½$ to $z = ¼$. In particular, the total buoyancy or weight deficiency (Scorer 1978) of the body force is the same in both experiments and the only difference is the location of the forcing. As anticipated in section 3b, there is no DPE in F22RL because convergence is strongest near the ground.

One of the reviewers suggested we pursue numerical experiments with vertically varying ambient rotation. Unfortunately, our numerical analog of a rotating tank precludes such an investigation because "imposing" $\Omega = \Omega(z)$ would be nonphysical. But we address this problem analytically in section 4 and also recall the results of Smith and Leslie (1978) for vortex formation driven by an axial body force aloft in a neutrally stratified atmosphere. They used open boundary conditions at the top and side, and performed three simulations in which the angular momentum was constant along the upper

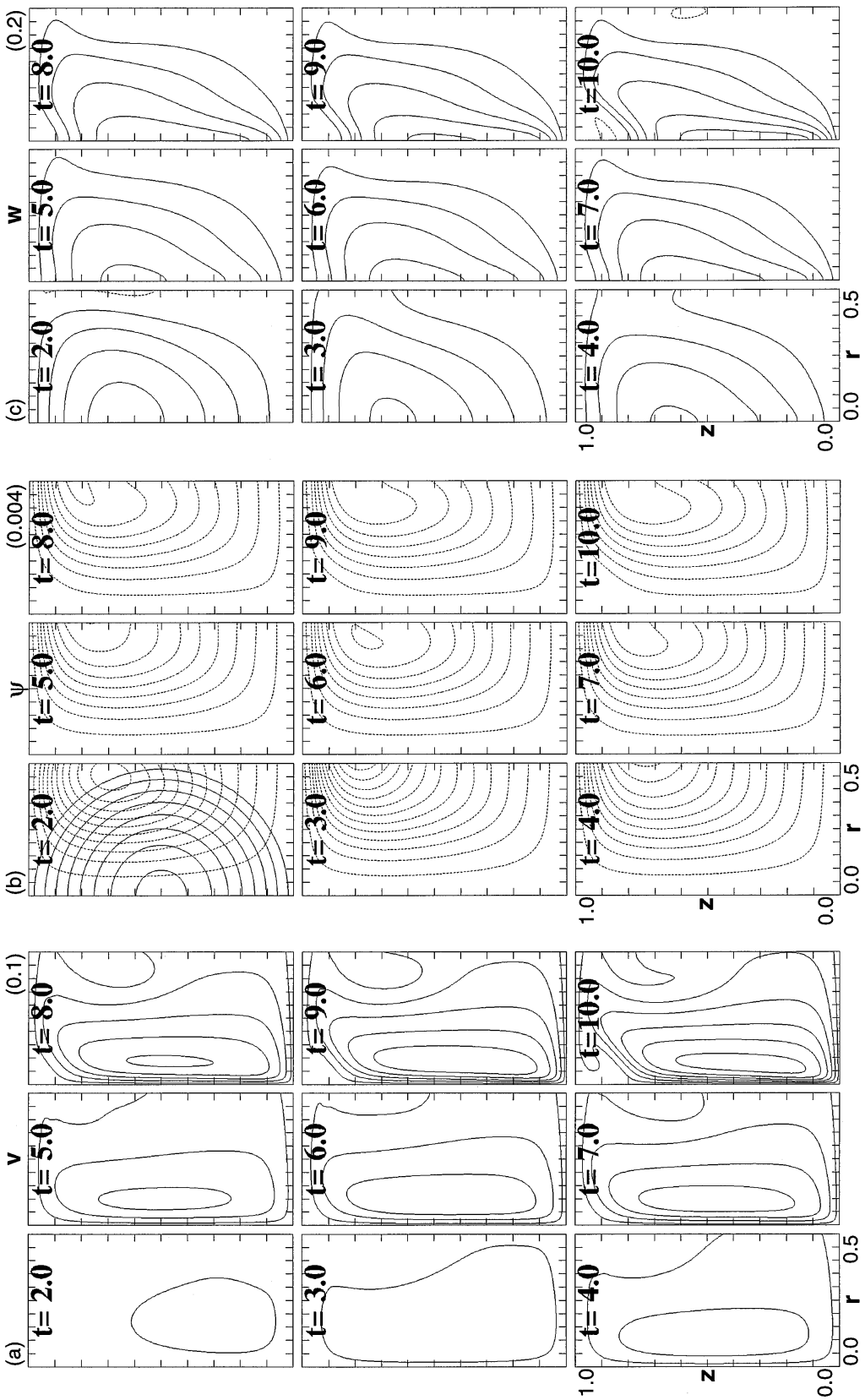

FIG. 5. As in Fig. 3 except for case N11R.

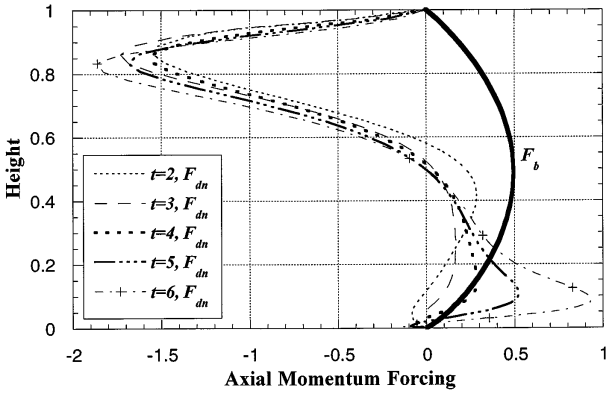

FIG. 6. As in Fig. 4 except for case N11R.

50%, 75%, and 100% of the side and zero in the lower part (if any) of the inflow. The respective steady states featured a suspended vortex aloft with divergence at the ground beneath it; a tornado that was weak, especially at the ground; and a strong tornado. Even though lack of low-level angular momentum in the first two cases was partly compensated for by high-angular-momentum air being drawn into the inflow from above, the vortices eventually reached a level during their descent where they drew on low-angular-momentum air. Consequently, they failed to become strong tornadoes.

4. Analytical model

A simple analytical model illustrates when a DPE is unnecessary for the establishment of a vortex in contact with the ground ($z = 0$). Equations (1)–(4) in a nonrotating frame ($\Omega \equiv 0$) may be reduced to the following two (azimuthal vorticity and angular momentum) equations in two unknowns (ψ and Γ):

$$\frac{\partial}{\partial t}\left(\frac{\eta}{r}\right) + 2J_{xz}\left(\psi, \frac{\eta}{r}\right) = \frac{1}{x^2}\frac{\partial \Gamma^2}{\partial z} - 2\frac{\partial b}{\partial x} + \frac{\nu}{x}\hat{\nabla}^2(r\eta), \tag{11}$$

$$\frac{\partial \Gamma}{\partial t} + 2J_{xz}(\psi, \Gamma) = \nu\hat{\nabla}^2\Gamma, \tag{12}$$

where

$$\eta \equiv -\frac{1}{r}\hat{\nabla}^2\psi, \tag{13}$$

the vector vorticity is $(\xi, \eta, \zeta) \equiv (-\partial\Gamma/r\partial z, \partial u/\partial z - \partial w/\partial r, \partial\Gamma/r\,\partial r)$, $x \equiv r^2$ is a new radial coordinate, the operator $\hat{\nabla}^2 \equiv 4x\partial^2/\partial x^2 + \partial^2/\partial z^2$, and the Jacobian operator

$$J_{xz}(\psi, \chi) \equiv \frac{\partial\psi}{\partial x}\frac{\partial\chi}{\partial z} - \frac{\partial\psi}{\partial z}\frac{\partial\chi}{\partial x}$$

(Lewellen 1971). We assume that $b\mathbf{k}$ is independent of r. This assumption is necessary for obtaining simple solutions. In effect, it makes the meridional circulation infinitely wide and removes the compensating downdraft to infinity. Although clearly unrealistic, this is defensible on the grounds of our finding that the mode of vortex formation is insensitive to bubble diameter. Because $b\mathbf{k}$ is a conservative force that does not generate vorticity, it could be absorbed into the pressure-gradient force. To obtain a logical partition of the total vertical force into VPGF and body force, we impose the boundary condition that the VPGF vanish at $r = \infty$. This is tantamount to assuming that the overall meridional flow is driven by buoyancy (or its surrogate, the body force), not by a large-scale VPGF. We also assume that the angular momentum is finite at $r = \infty$. Note that for axisymmetric flow the vortex lines lie in surfaces of constant angular momentum, just as the 3D velocity vectors lie in stream surfaces. The quantity η/r appearing on the left side of (11) is conserved in the absence of the centrifugal, buoyancy, and viscous torques on the right side of (11). To see why this quantity is conserved, consider a material (nonentraining) vortex ring. Because the volume and strength of the ring are invariant, the vorticity must increase with r to compensate for the $1/r$ dependence of cross sectional area.

We choose the steady streamfunction $\psi = axz^n$, which is associated with the azimuthal vorticity $\eta = -an(n - 1)rz^{n-2}$, and horizontal convergence $\delta = 2anz^{n-1}$. Here, a (>0) is a constant with units of $m^{1-n}\ s^{-1}$. This streamfunction is an exact steady-state solution of (11) when $n = 1$ or 2, if $\partial\Gamma/\partial z = 0\ \forall t$. We allow the tangential velocity to be unsteady, and deduce its evolution in time from an initial state that represents a larger-scale height-independent vortex.

First, consider $n = 1$. In this case, the streamlines are cubic hyperbolas (Fig. 11a) and $\eta \equiv 0$. The meridional flow is identical to that of a Burgers(1948)–Rott(1958) vortex, identical also to irrotational, axisymmetric flow near a stagnation point, and similar to the throughflow in the convergence region of Ward's (1972) tornado chamber (see Rotunno 1977). Because the inflow and tangential velocities are independent of z, the vortex lines remain vertical and the surfaces of constant angular momentum remain cylindrical [the latter only requires $u \neq u(z)$]. In Rotunno's numerical simulations of the tornado chamber, this indeed happens at low levels for free slip at the ground. [Above the inflow layer the angular momentum surfaces slope outward with height owing to the upward advection of Γ along the chamber's outer wall.] Hence, there is no DPE in the numerical simulations of the laboratory experiment. Since the swirl has no influence on the meridional flow, ψ is an exact solution of (11) even with rotation. The solution for pressure,

$$\phi(r, z) = \phi(0, 0) - \frac{a^2}{2}(r^2 + 4z^2) + \int_0^z b\,dz + \int_0^r \frac{v^2}{r}\,dr, \tag{14}$$

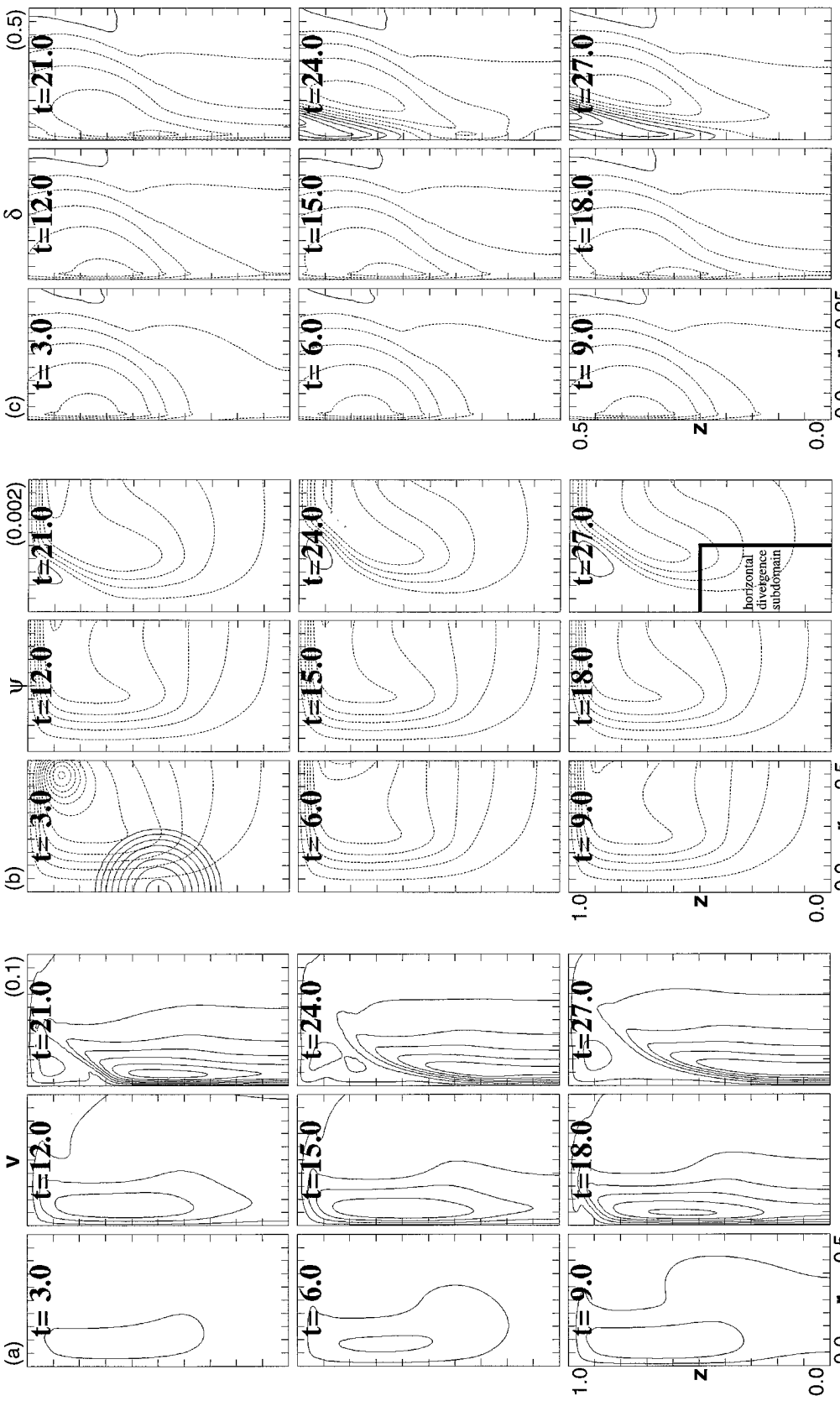

FIG. 7. As in Fig. 3 except for case F22R and with contours of horizontal divergence $\delta = 1/r(\partial/\partial r)(ur)$ plotted in (c). In (c), the plotting window is ($0 \le r \le 0.25$, $0 \le z \le 0.5$).

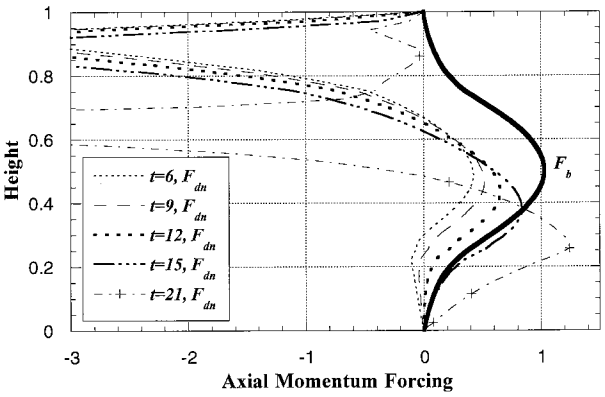

FIG. 8. As in Fig. 4 except at times $t = 6$, 9, 12, 15, and 21, for case F22R.

shows that the swirl has no effect on the throughflow because temporal increases in centrifugal force are exactly counterbalanced by increases in the inward radial pressure-gradient force. The condition that the VPGF $= 0$ at $r = \infty$ implies that $b\mathbf{k} \equiv 4a^2z\mathbf{k}$ and that the VPGF $\equiv 0$ everywhere. If diffusion of angular momentum is ignored, angular momentum is conserved and (12) has the solution

$$\Gamma(r, t)=\Gamma(r_0, 0), \ \forall z, \tag{15}$$

where $(r_0, z_0)=(re^{at}, ze^{-2at})$ is the initial location of the parcel that is at (r, z) at time t. This equation states that the evolution of the swirling component of the flow is determined solely by the initial angular momentum and the parcel trajectories. Rott (1958) found an exact solution of (12), which is preferable to (15) because the inclusion of diffusion allows asymptotic evolution to a steady state (the Burgers–Rott vortex), in which there is a balance between inward advection and outward diffusion of angular momentum. His transient solution is

$$\Gamma(x, t) = \Gamma_\infty\left\{1 - \exp\left[-\frac{1.257x}{x_c(t)}\right]\right\}, \tag{16}$$

where $x_c(t)$, the square of the core radius $r_c(t)$ at time t is given by

$$x_c(t) = x_c(\infty)(1 + \beta e^{-2at});$$

$$x_c(\infty) = 1.257\left(\frac{2\nu}{a}\right), \tag{17}$$

and the parameter $\beta \equiv (x_c(0)/x_c(\infty)) - 1$. The maximum tangential velocity, located at $r_c(t)$, is $v_c(t) = 0.715\Gamma_\infty \div r_c(t)$. The core radius moves inward with the speed

$$\frac{dr_c(t)}{dt} = -ar_c(t)\frac{\beta e^{-2at}}{1 + \beta e^{-2at}}. \tag{18}$$

Thus, for large β the core radius advects inward with virtually no retardation by diffusion initially (Fig. 11). This exact solution suffers from unbounded meridional flow at infinity but otherwise satisfies reasonable boundary conditions (e.g., the axial symmetry conditions, free-slip flat ground, and constant circulation at $r = \infty$). Thus, it is a good illustration of vortex formation without a DPE.

We now consider the $n = 2$ case. Here the streamlines are hyperbolas, $\eta = -2ar$, and, in the absence of swirl,

$$\phi(r, z) = \phi(0, 0) - 2a^2z^4 + \int_0^z b\, dz + 4\nu az$$

is independent of r. The steady body force that drives and maintains the convergent meridional flow in the face of intensifying swirling flow is given by $b\mathbf{k} \equiv (8a^2z^3 - 4\nu a)\mathbf{k}$. For this body force, the VPGF vanishes in regions of uniform angular momentum (as shown below), as well as at $r = \infty$. Note that this body force is a much stronger function of height than the one in the $n = 1$ case (z^3 compared to z). Our model quickly becomes unrealistic when $n \neq 1$ because the through and swirling flows are coupled. Vertical variations in centrifugal force develop and affect the azimuthal vorticity and hence the streamfunction, violating the assumption that the throughflow is steady. However, the model is sufficient for our purpose of illustrating different ways of vortex development because the modification of the ψ field by the swirling flow occurs primarily near a concentrated vortex core (Lewellen 1971, 19) and because we can deduce qualitatively from imbalances in the equations governing the throughflow how the streamlines will adjust to the intensifying vortex. The initial ψ field may be regarded as the primary meridional circulation and the modifications to ψ, as the secondary circulation induced by the contracting vortex.

Since diffusion of angular momentum is negligible initially (as above) and the throughflow changes slowly at first, the inviscid solution of (12) (for fixed ψ),

$$\Gamma(r, z, t) = \Gamma(r_0, z_0, 0) = \Gamma(r[1 + 2azt], z/[1 + 2azt], 0) \tag{19}$$

suffices as a beginning approximation. Initially cylindrical surfaces of constant angular-momentum are deformed into surfaces of revolution that taper upward (as do the surfaces of revolution generated by the core-radius curves in Fig. 12) because the inflow increases with height. The associated centrifugal torques act to produce positive azimuthal vorticity—that is, of opposite sign to the vorticity of the primary flow. From a vorticity dynamics perspective, the vortex lines, which initially spiral upward around cylindrical surfaces in the negative θ direction, are frozen in the fluid. The trajectory of a parcel initially at (r_0, θ_0, z_0) is given by

$$(r, \theta, z) = \left[r_0(1 - 2az_0t), \ \theta_0 + \frac{\Gamma(r_0)}{r_0^2}\frac{t}{1 - 2az_0t}, \ \frac{z_0}{1 - 2az_0t}\right], \quad t < (2az_0)^{-1}. \tag{20}$$

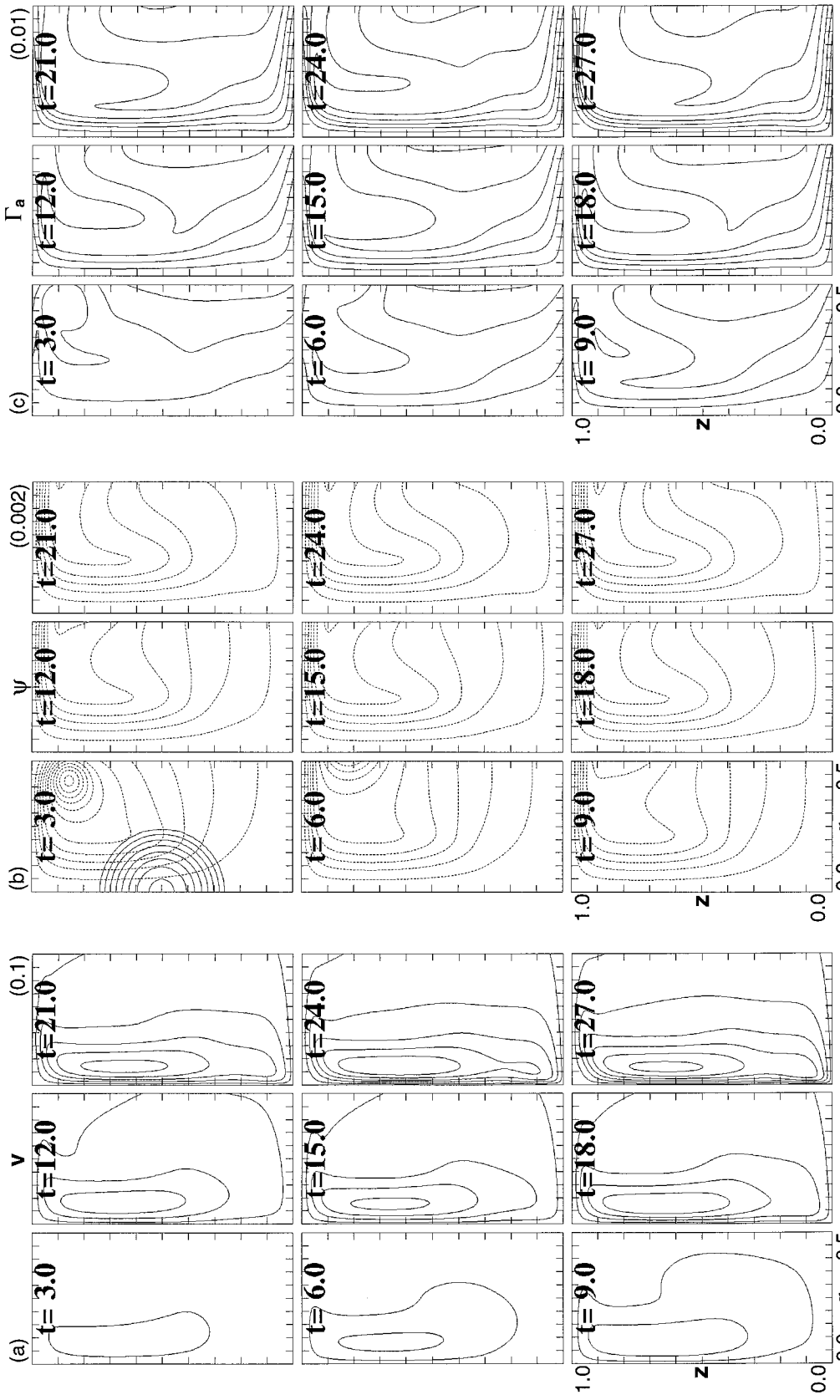

FIG. 9. As in Fig. 3 except for case N22R and with contours of absolute angular momentum plotted in (c).

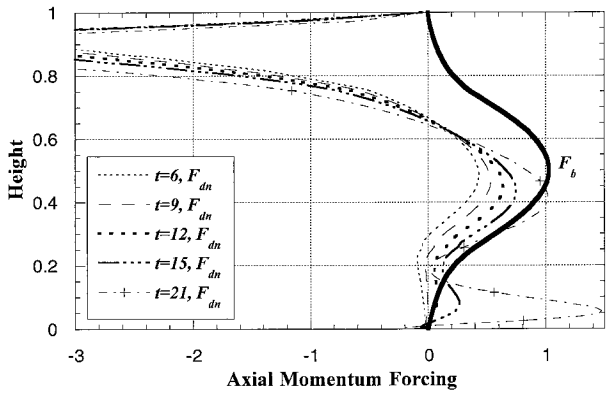

FIG. 10. As in Fig. 4 except at times t = 6, 9, 12, 15, and 21, for case N22R.

Thus, the vortex lines are stretched, and tilted inward and toward the positive θ direction. Rotunno (1980) deduced a similar configuration for vortex lines in the boundary layer of a convective swirling flow (see his Fig. 3b).

The azimuthal vorticity can be decomposed into shear and curvature components. In and downstream of the region of positive azimuthal vorticity generation, there is a net increase in curvature plus shear vorticity by definition (i.e., at each point there has to be either gains in both components or a gain in one component has to dominate a loss in the other). Increasing azimuthal vorticity is consistent with increasing axial updraft and low-level inflow at low levels (increasing shear vorticity with minor decrease in curvature vorticity) and more abrupt bending of the streamlines as the flow turns the corner (increasing curvature vorticity in this region). Such a

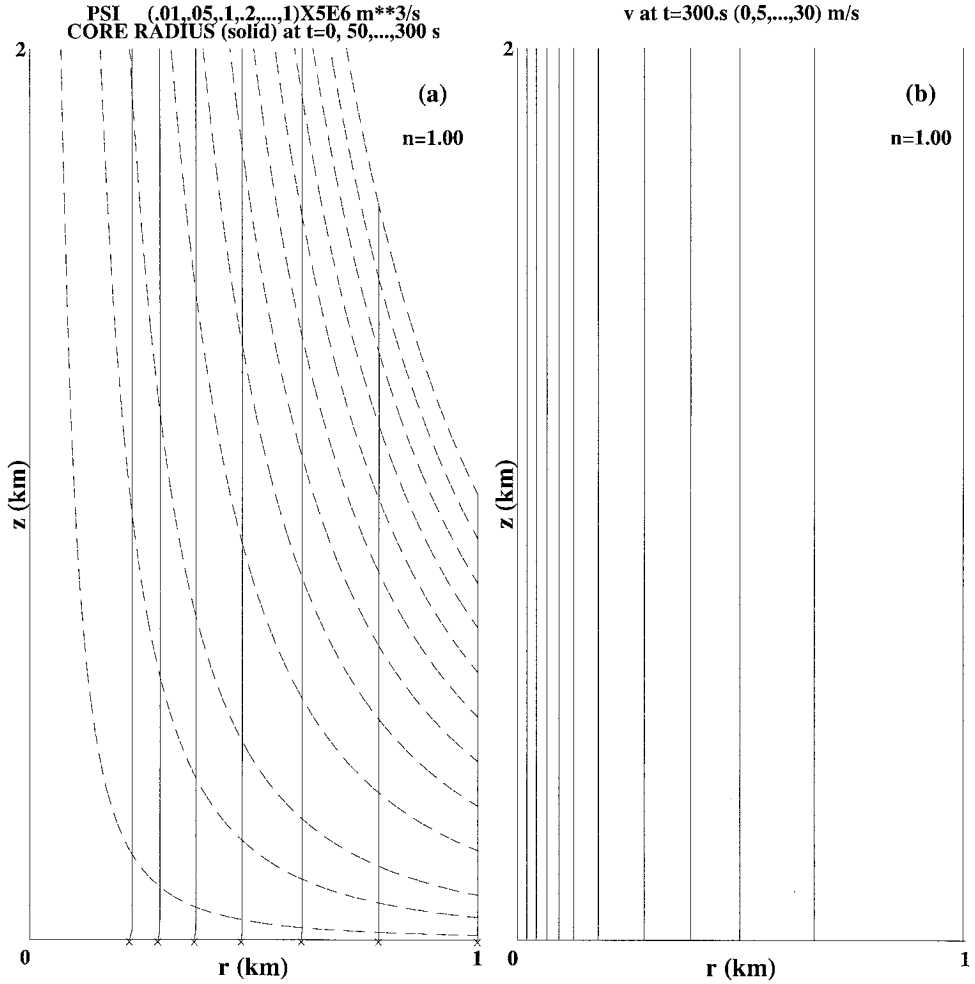

FIG. 11. Here, n = 1 case ($\psi = axz$). Rott's analytical solution in the window ($0 \le r \le 1$ km, $0 \le z \le 2$ km) for convergence $2a = 10^{-2}$ s^{-1}, $r_c(0) = 1$ km, $r_c(\infty) = 50$ m, $\Gamma_\infty = 10^4$ m^2 s^{-1} (thus $\beta = 399$, $\nu = 4.97$ m^2 s^{-1}). (a) The (0.01, 0.05, 0.1, 0.2, . . . , 1.0) $\times$ 5 $\times$ 10^6 m^3 s^{-1} streamfunction contours (dashed), and core radius $r_c(t)$ (solid) as function of height at t = 0, 50, . . . , 300 s. The x's along the r axis denote the core-radii values in the inviscid limit. (b) The (0, 5, . . . , 30) m s^{-1} contours of tangential velocity at t = 300 s.

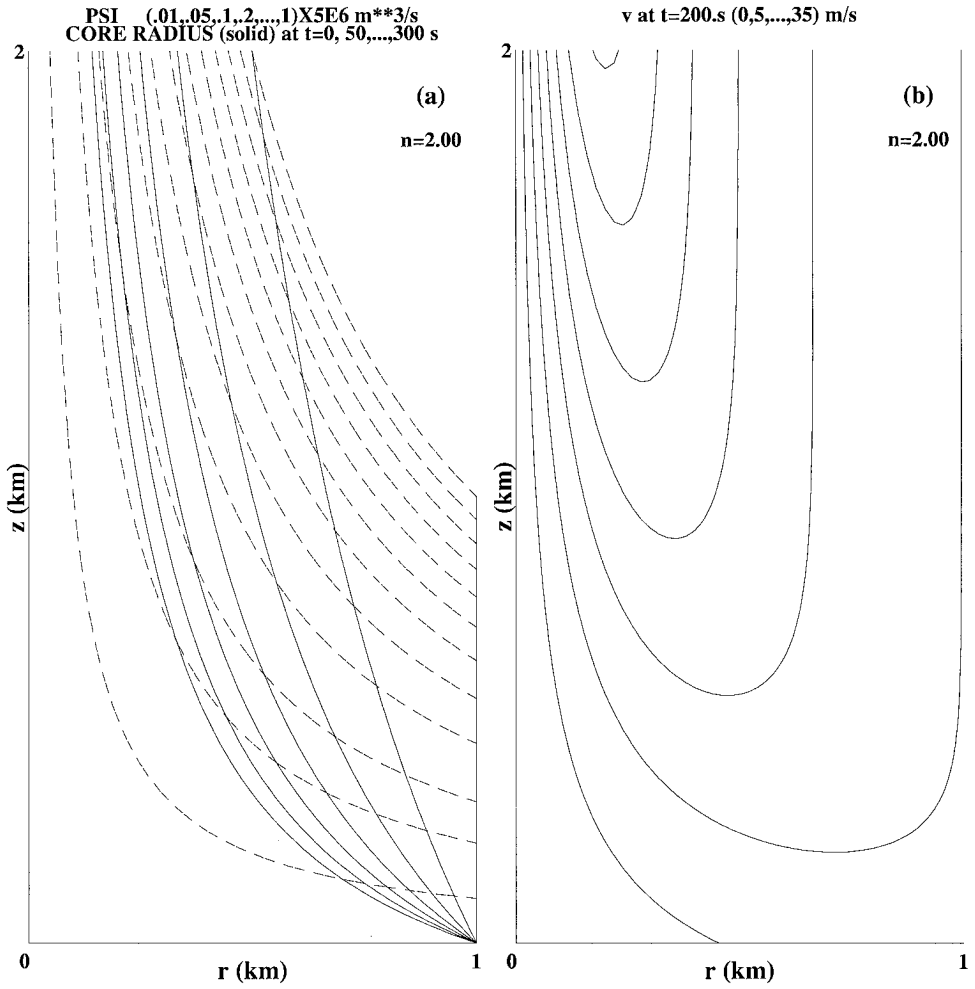

FIG. 12. Here, $n = 2$ case ($\psi = axz^2$). The convergence, $4az = 10^{-2}$ s^{-1} at $z = 500$ m. The initial tangential velocity field is the same as in the $n = 1$ case. (a) As in Fig. 11a except the x's are omitted because they are superfluous. (b) Here, (0, 5, . . . , 35) m s^{-1} contours of tangential velocity at $t = 200$ s. The core radius and tangential velocity are computed in this case by neglecting diffusion of angular momentum and changes in the streamfunction.

secondary circulation would increase the transport of angular momentum toward the axis at low levels and so contribute to a DPE. This scenario is supported by the following argument.

We assume that the initial swirling flow is a height-independent Rankine combined vortex and that the total flow is in cyclostrophic balance. The latter is possible because the advection terms in the radial momentum equation cancel initially. Then, the starting pressure field is given by

$$\phi_0(x) = \begin{cases} \phi_\infty - \Omega_0^2 x_{c0}^2/2x, & x \geq x_{c0} \\ \phi_\infty - \Omega_0^2 x_{c0} + \dfrac{1}{2}\Omega_0^2 x, & x \leq x_{c0}, \end{cases} \tag{21}$$

where Ω_0 and $x_{c0}^{1/2} \equiv r_{c0}$ are the initial rotation rate and radius of the vortex core, and ϕ_∞ is the pressure at radial infinity (all independent of height). We assume that the pressure at infinity remains constant, that is, $\phi(\infty, z, t) = \phi_\infty$.

Owing to the conservation of angular momentum, the core radius is advected inward. If ψ is held fixed, the core radius is the following function of the similarity variable $s \equiv 2azt$,

$$x_c^{1/2}(s) \equiv r_c(s) = \frac{r_{c0}}{1 + s}, \tag{22}$$

and the angular momentum is given by

$$\Gamma(x, s) = \begin{cases} \Omega_0 x(1 + s)^2, & x \leq x_c(s) \\ \Omega_0 x_c(1 + s)^2, & x \geq x_c(s) \end{cases} \tag{23}$$

from (19) and (20). Therefore, for fixed ψ, the vortex remains a Rankine combined vortex at each level with

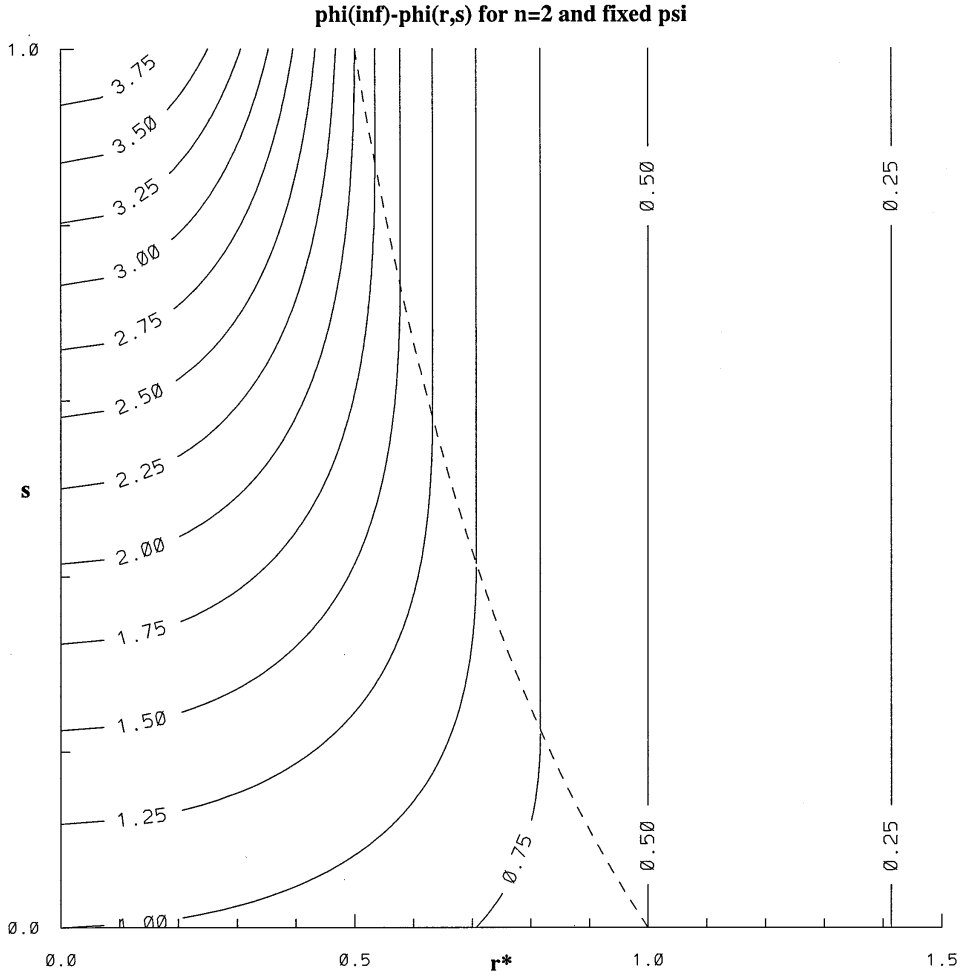

FIG. 13. The pressure field, as a function of r and $s \equiv 2azt$, that arises when the streamfunction is not allowed to adjust to the changing swirling flow in the $n = 2$ case. The abscissa, r^*, is the radial coordinate nondimensionalized by r_{c0}, the initial core radius. The contour labels are values of $\phi_\infty - \phi(r, s)$ normalized by $\Omega_0^2 r_{c0}^2$, the axial pressure deficit at $t = 0$. The dashed line is the nondimensional core radius as a function of s. Upward pressure-gradient forces develop in the vortex core at $t > 0$—that is, for $s > 0$—and modify the streamfunction field as described in the text.

an amplifying solid-body rotation, $\Omega_0(1 + s)^2$, and contracting core radius, $r_{c0}/(1 + s)$.

We now compute the imbalance in the vertical equation of motion that results from not allowing the streamfunction to adjust to the changing swirl field. The pressure field still can be determined from the cyclostropic relationship because ψ is held fixed. It is given by

$$\phi(x, s) = \begin{cases} \phi_\infty - \Omega_0^2 x_{c0}^2/2x, & x \geq x_{c0}/(1 + s)^2 \\ \phi_\infty - \Omega_0^2 x_{c0}(1 + s)^2 + \dfrac{1}{2}\Omega_0^2 x(1 + s)^4, & \\ & x \leq x_{c0}/(1 + s)^2 \end{cases} \tag{24}$$

(see Fig. 13). Note that the VPGF vanishes outside the vortex core. Within the core, there is an unbalanced upward pressure-gradient force which is greatest on the axis. Thus, the meridional flow must adjust by developing an axial jet ($\partial w/\partial r < 0$), and, by continuity, increasing inflow at low levels. These changes represent an increase in η (as deduced above) and the drawing in of the streamlines depicted in Fig. 14b (as surmised above).

Last we consider the case where the flow is inviscid, initial convergence is constant with height ($n = 1$), and the initial swirl flow is a height-dependent Rankine combined vortex of radius r_{c0} (height independent) and outer angular momentum $\Gamma_\infty(z_0) \geq 0$, $\forall z_0$ where the Lagrangian coordinates $(r_0, z_0) = (re^{at}, ze^{-2at})$. Once again, the tangential flow remains a Rankine combined vortex at each level as long as ψ is held fixed. For the $n = 1$ case we must include the inertial force, $a^2 r$, in addition to the centrifugal and pressure-gradient forces, in the force balance in the radial momentum equation. Proceeding as before, we find that the unbalanced vertical-pressure gradient force is

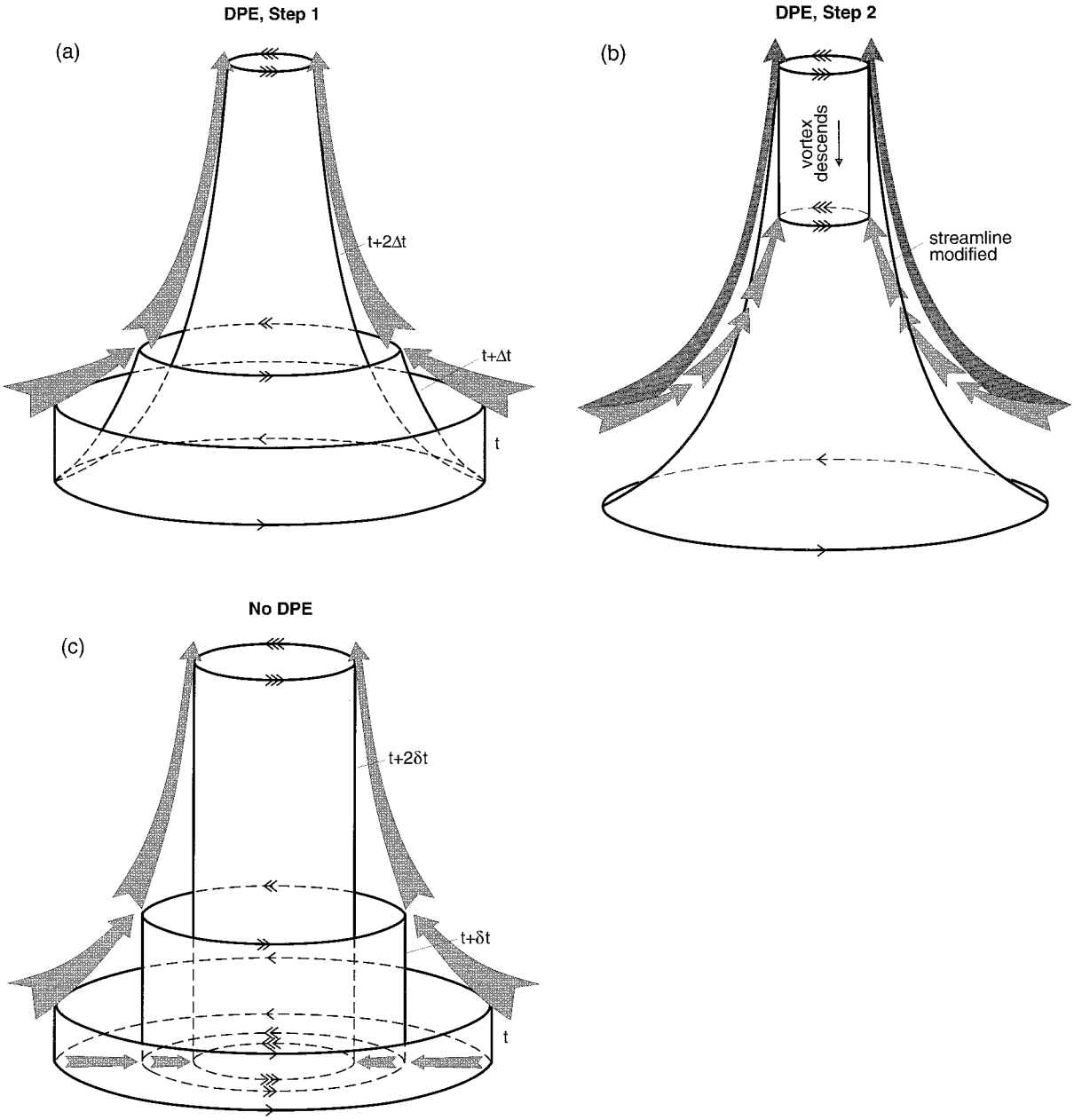

FIG. 14. Idealization of two modes of vortex formation within a rotating updraft. Number of barbs on wind arrows indicates strength of swirling wind component. (a) Step 1 of vortexgenesis for case when maximum convergence is aloft and surface inflow is weak (or absent as depicted here). Initial cylindrical vortex tube is deformed by meridional flow (depicted by bold streamline) as shown after time $t + \Delta t$ and $t + 2\Delta t$, resulting in increased rotation aloft. (b) Step 2. Vortex begins to build down by dynamic pipe effect (see text) as it modifies streamlines (dashed) in its vicinity. In practice, steps 1 and 2 occur concurrently rather than consecutively, but step 2 only becomes a significant effect as high-angular-momentum parcels reach small radii. The vortex will contact the ground only through the slow DPE process. (c) As in (a) but for vortexgenesis when convergence is constant with height. In this case, the vortex tube is stretched but remains cylindrical, resulting in simultaneous increase in rotation throughout a large depth. Streamlines are unmodified (assuming a free-slip lower boundary).

$$-\frac{\partial \phi}{\partial z}(x^*, z_0) = \begin{cases} \dfrac{1}{x_{c0}} \dfrac{\partial \Gamma_\infty^2}{\partial z_0} \dfrac{1}{2x^*}, & x^* \geq 1 \\ \dfrac{1}{x_{c0}} \dfrac{\partial \Gamma_\infty^2}{\partial z_0} \left(1 - \dfrac{x^*}{2}\right), & x^* \leq 1, \end{cases} \tag{25}$$

where $x^* \equiv x/x_c$. If Γ_∞^2 decreases monotonically with height, the VPGF is downward in opposition to the body force, and the vortex core tends to draw down low-angular-momentum air from higher levels, a mitigating effect on vortex intensity. When Γ_∞^2 increases monoton-

ically with height, the VPGF is upward and the secondary flow has positive azimuthal vorticity. As the vortex contracts, it draws on air from progressively lower heights (because $z_0 = ze^{-2at}$) with progressively less angular momentum. As deduced previously by Smith and Leslie (1978), this results in a weak tornado at ground level, or even a vortex suspended aloft if near-ground ambient angular momentum is absent.

The analytical model suggests that a DPE occurs only when the influx of angular momentum is greatest aloft. If the initial angular momentum field is independent of height, then the tornado-scale vortex forms aloft and works its way down to the ground by a DPE when $n > 1$ (i.e., when the convergence δ increases with height); it forms at all heights simultaneously when $n = 1$ (δ constant); and it forms from the ground up when $0 < n < 1$ (δ decreases with height). {Note that we do not present an $n < 1$ case here because the solutions are singular. Even though the streamfunction (i.e., mass flux) is finite, the radial inflow is infinite at the ground so surface parcels reach the axis in zero time and then turn upward. This limits the solution region to $z > [2a(1 - n)t]^{1/(1-n)}$.}

When the initial swirl is constant with height, the vertical forces do not have to be greatest at the ground for there to be no DPE, but they do have to induce surface convergence that is at least equal to the convergence aloft. Thus, the height dependence of the convergence seems to be a simpler discriminant than the vertical distribution of the vertical forces. If, on the other hand, the convergence is held constant with height, and the initial angular velocity is allowed to vary monotonically with height, then a DPE will occur only when the initial swirl increases upward and is significant at the ground.

5. Summary and discussion

There are two distinct modes of tornado development. In the first and archetypal, which we label mode I, the embryonic tornado develops aloft (3 to 4 km) in the parent storm and slowly builds downward to the ground (and upward by vorticity advection to as high as 12 km for large tornadoes), with the tornadic vortex signature (TVS) on radar foreshadowing tornado touchdown by as much as 20 min. In mode II tornadogenesis, the embryonic tornado (and associated TVS) forms either simultaneously over the lowest ~2 km or very near the ground and then rapidly contracts radially (and stretches upward) into a tornado with little advance warning. Hence, the maximum achievable lead time of tornado warnings depends greatly on the particular mode. Because mode I tornadogenesis was observed first (e.g., Brown et al. 1978), the importance of mode II formation is being recognized only gradually by research and operational meteorologists.

From our numerical and analytical models of a mesocyclone, we conclude that the mode of development depends on the trajectories of high-angular-momentum air during tornadogenesis. If ''ambient'' (i.e., mesocyclonic) vertical vorticity and/or radial inflow are greater aloft than next to the ground, high-angular-momentum air arrives near the axis first aloft and mode I genesis ensues (Fig. 14a). In the case of insufficient low-level rotation, the vortex remains aloft (Smith and Leslie 1978). In the case of insignificant near-ground convergence associated with the larger-scale flow, the embryonic vortex must develop its own low-level convergence in order to build itself downward (assuming low-level rotation is sufficient). It does so by the dynamic pipe effect (DPE), a type of bootstrap process (Fig. 14b). Centrifugal forces prevent air from entering the vortex through its sides, and in this respect, the vortex acts like a pipe. As air is drawn into the lower end of the vortex core by the partial vacuum there, it spins faster, becoming part of the pipe. The pipe builds downward in this fashion, drawing air from and intensifying at progressively lower levels, thereby increasing low-level convergence.

When ambient vorticity and radial inflow are constant with height, high-angular-momentum air approaches the axis at the ground and aloft simultaneously. The vortex in this case forms nearly independently with height over the lowest few kilometers (mode II), precluding a need for a DPE (see Fig. 14c). Analogously, if ambient vertical vorticity and radial inflow are maximized near the ground, the vortex forms from the ground upward. Because a DPE is again precluded, this type of genesis is consistent with the mode II taxonomy.

In applying the results of our numerical experiment to the genesis of various convective vortices in the atmosphere, it is natural to interpret the body force as a buoyancy force computed from a sounding representing an idealized, time-independent, horizontally homogeneous ''environment'' or basic state in hydrostatic balance. The partitioning of upward forces into buoyancy and perturbation pressure-gradient forces depends on this arbitrary choice of basic state, which excludes, for instance, the rain-cooled air produced by parent storms. Clearly, buoyancy should be viewed as relative to a base state rather than absolute. Cool air that is negatively buoyant relative to the environment may act as if it is ''positively buoyant'' (i.e., rise) when in close proximity to very cold air. Because perturbation pressure-gradient forces are capable of accelerating even negatively buoyant air upward, it is prudent to regard the body force as a surrogate for the overall upward forces driving the larger-scale circulation (excluding forces arising from the tornadic vortex itself). Ward's tornado chamber, where the vortices are generated by mechanical lifting rather than buoyancy forces, demonstrates the importance of the larger-scale pressure forces (Ward 1972).

Before considering atmospheric vortices, we recall Rotunno's (1977) numerical simulation of Ward's model, in which a DPE does not occur. The low-level convergence and rotation in this simulation are independent

of height. This lack of a DPE corroborates with our findings about DPE absence [as do, e.g., the simulations of Smith and Leslie (1978) with our findings about DPE presence] and therefore gives us confidence in applying our results to the atmosphere.

Dust devils (Morton 1966), waterspouts (Golden 1974), landspouts (Brady and Szoke 1989), and cold-air funnel clouds (Cooley 1978) all form when environmental lapse rates near the ground are either superadiabatic or dry adiabatic. Dust devils, waterspouts, and landspouts may all be the result of updrafts stretching pre-existing low-level vortices (which may originate from shearing instability of low-level boundaries). Although waterspouts and landspouts may form in cloud shadow and hence not directly in a region of superadiabatic lapse rate, they are located on gust fronts or other convergence lines. Thus, significant low-level upward forces [either buoyancy or vertical pressure gradient force (VPGF) or both] and low-level rotation may be present throughout the formation of dust devils, waterspouts, and landspouts and we do not expect the DPE to be essential in these cases. Similarly, we also do not expect a significant DPE for gustnadoes, which are short-lived dust whirls or weak tornadoes that spin up from parent circulations of small diameter ($<$1 km) and shallow depth ($<$2 km) along thunderstorm gust fronts or other wind shear lines (Wilson 1986). On the other hand, cold-air funnel clouds rarely contact the ground, suggesting that they build downward slowly through a DPE and that there is probably a lack of low-level rotation.

In contrast to the above vortices, (archetypal) supercell tornadoes generally occur later in the ''parent storm's'' life when pools of rain-cooled air may be extensive. The maximum buoyancy in a typical supercell storm is in the upper troposphere and the lapse rate below the rotating wall cloud (from which the tornado usually emanates) is stable. Supercell tornadoes develop in moderately cool air just behind the gust front. In the first 2 h of the storm's life, strong surface outflow winds have not yet developed, low-level forces, surface convergence, and low-level rotation on the mesocyclone scale are all relatively weak and the DPE should play an important role in tornado formation. TVS observations often confirm this deduction for the first tornado produced by the storm, which usually has a TVS aloft 10 min or more prior to tornado touchdown. At the time the first TVS forms aloft, the mesocyclone's rotation is stronger at low-to-mid levels than near the ground because at this stage it originates primarily from tilting by the updraft of environmental streamwise vorticity (Davies-Jones 1984). Doppler radar observations reveal that the TVS approaches the ground only after mesocyclonic rotation near the ground intensifies and becomes larger than the rotation further aloft. The near-ground cyclonic rotation may develop in the left side (looking downwind) of the rain-cooled downdraft as a result of tilting of baroclinic vorticity and then intensify as the cyclonically spinning air reaches close to the ground, is entrained into the side of the updraft and stretched vertically (Davies-Jones and Brooks 1993; Davies-Jones 1996b). If the local vertical stability in the lowest kilometer is too large, the vortex is unable to lift the dense air beneath it, and the DPE ceases, resulting in a tornadic vortex (sometimes manifest as a ''funnel cloud'') that stays aloft (Leslie and Smith 1978). Similarly, a suspended vortex may also result if near-ground mesocyclogenesis ''fails'' (Brooks et al. 1993) because of insufficient low-level rotation (Smith and Leslie 1978).

The TVSs associated with the second and subsequent tornadoes in a cyclic supercell storm may also form aloft and descend but often begin instead as shallow, weak, low-level features (NOAA 1990). Each of these tornadoes typically occurs in a new mesocyclone that develops rapidly over a large depth above a bulge in the gust front formed by strong cool winds sweeping around the previous mesocyclone as it occludes (Burgess et al. 1982). At the gust-front bulge, there exists strong convergence between relatively cool, high-momentum air and warm inflowing air. Here, VPGFs are significant and capable of lifting even cool, fairly stable air. The presence of significant low-level forcing and preceding ground-level rotation probably explains why the DPE often is not observed in the genesis of successive supercell tornadoes.

Last, we consider hurricane tornadoes. These are spawned by shallow minisupercell storms that form in the low CAPE but strongly sheared environments found in landfalling hurricanes (McCaul and Weisman 1996). Even though cold pools are less pronounced in these minisupercells—compared to supercells in the Great Plains—because of the absence of very dry air at midlevels in hurricanes, low-level forcing is still significant. Buoyancy forces are weak with maximum buoyancy located around 3–4 km (i.e., below midlevel in the storm, which is typically 10 km high). The maximum vertical velocity is even lower, at around 2 km, owing to intense low-level VPGF (McCaul and Weisman 1996) induced by the interaction of the updraft with strong low-level shear (Rotunno and Klemp 1982; Brooks and Wilhelmson 1993; Davies-Jones 1996a) and other dynamic effects. Given that low-level convergence is significant, we have to consider the ambient rotation to determine whether or not a DPE is needed for tornado formation. In the lowest kilometer, there is abundant low-level horizontal vorticity associated with large environmental shear. Thus, tilting and stretching of environmental vorticity by the strong low-level updraft gradients should produce appreciable vertical vorticity in rising air at fairly low levels but not directly next to the ground where tilting is negligible (Davies-Jones and Brooks 1993). The same near-surface baroclinic mesocyclogenetic processes that occur in supercells (Rotunno and Klemp 1985; Davies-Jones and Brooks 1993) can occasionally take place in hurricane minisupercells despite the relative lack of dry midlevel air (McCaul

and Weisman 1996). Thus, we conclude that hurricane tornadoes may exhibit either mode of tornadogenesis, depending mainly on the relative strengths of near-surface and low-to-midlevel mesocyclonic rotations. If the TVS develops aloft, it probably does so at relatively low heights (around 2 km).

Acknowledgments. We thank Dr. Brian Fiedler for the use of his model, Drs. Harold Brooks and Erik Rasmussen for critiquing a draft of this paper, and Ms. Joan O'Bannon for drafting Fig. 14. Part of this research was inspired by a discussion with Dr. Richard Rotunno, whose comments along with those of the two other reviewers are appreciated. Participation in the Verification of the Origins of Rotation in Tornadoes Experiment (VORTEX) helped the authors to reach their conclusions. This work was performed while one of the authors (R.J.T.) was a National Research Council-NOAA Postdoctoral Research Associate.

REFERENCES

Brady, R. H., and E. J. Szoke, 1989: A case study of nonmesocyclone tornado development in northeast Colorado: Similarities to waterspout formation. *Mon. Wea. Rev.,* **117,** 843–856.

Brooks, H. E., and R. B. Wilhelmson, 1993: Hodograph curvature and updraft intensity in numerically modeled supercells. *J. Atmos. Sci.,* **50,** 1824–1833.

———, C. A. Doswell III, and R. Davies-Jones, 1993: Environmental helicity and the maintenance and evolution of low-level mesocyclones. *The Tornado: Its Structure, Dynamics, Prediction, and Hazards, Geophys. Monogr.,* No. 79, Amer. Geophys. Union, 97–104.

Brown, R. A., L. R. Lemon, and D. W. Burgess, 1978: Tornado detection by pulsed Doppler radar. *Mon. Wea. Rev.,* **106,** 29–39.

Burgers, J. M., 1948: A mathematical model illustrating the theory of turbulence. *Adv. Appl. Mech.,* **1,** 197–199.

Burgess, D. W., V. T. Wood, and R. A. Brown, 1982: Mesocyclone evolution statistics. Preprints, *12th Conf. on Severe Local Storms,* San Antonio, TX, Amer. Meteor. Soc., 422–424.

Burgraff, O. R., K. Stewartson, and R. Belcher, 1971: Boundary layer induced by a potential vortex. *Phys. Fluids,* **14,** 1821–1833.

Cooley, J. R., 1978: Cold air funnel clouds. *Mon. Wea. Rev.,* **106,** 1368–1372.

Davies-Jones, R. P., 1973: The dependence of core radius on swirl ratio in a tornado simulator. *J. Atmos. Sci.,* **30,** 1427–1430.

——, 1984: Streamwise vorticity: The origin of rotation in supercell storms. *J. Atmos. Sci.,* **41,** 2991–3006.

——, 1986: Tornado dynamics. *Thunderstorm Morphology and Dynamics.* 2d ed. E. Kessler, Ed., University of Oklahoma Press, 197–236.

——, 1996a: Inclusion of boundary conditions on pressure in conceptual models of updraft-environment interaction. Preprints, *18th Conf. on Severe Local Storms,* San Francisco, CA, Amer. Meteor. Soc., 713–717.

——, 1996b: Formulas for the barotropic and baroclinic components of vorticity with applications to vortex formation near the ground. Preprints, *Seventh Conf. on Mesoscale Processes,* Reading, United Kingdom, Amer. Meteor. Soc., 14–16.

——, and H. Brooks, 1993: Mesocyclogenesis from a theoretical perspective. *The Tornado: Its Structure, Dynamics, Prediction, and Hazards, Geophys. Monogr.,* No. 79, Amer. Geophys. Union, 105–114.

Fiedler, B. H., 1993: Numerical simulation of axisymmetric tornadogenesis in buoyant convection. *The Tornado: Its Structure, Dynamics, Prediction, and Hazards, Geophys. Monogr.,* No. 79, Amer. Geophys. Union, 41–48.

——, 1994: The thermodynamic speed limit and its violation in axisymmetric numerical simulations of tornado-like vortices. *Atmos.–Ocean,* **32,** 335–359.

——, 1995: On modelling tornadoes in isolation from the parent storm. *Atmos.–Ocean,* **33,** 501–512.

——, and R. Rotunno, 1986: A theory for the maximum windspeeds in tornado-like vortices. *J. Atmos. Sci.,* **43,** 2328–2340.

Golden, J. H., 1974: Scale-interaction implications for the waterspout life cycle. Part II. *J. Appl. Meteor.,* **13,** 693–709.

Klemp, J. B., and R. Rotunno, 1983: A study of the tornadic region within a supercell thunderstorm. *J. Atmos. Sci.,* **40,** 359–377.

Leslie, L. M., 1971: The development of concentrated vortices: A numerical study. *J. Fluid Mech.,* **48,** 1–21.

——, and R. K. Smith, 1978: The effect of vertical stability on tornadogenesis. *J. Atmos. Sci.,* **35,** 1281–1288.

Lewellen, W. S., 1971: A review of confined vortex flows. NASA Contractor Rep. NASA CR-1772, 219 pp. [Available from the National Technical Information Service, Springfield, VA 22151.]

McCaul, E. W., Jr., and M. L. Weisman, 1996: Simulations of shallow supercell storms in landfalling hurricane environments. *Mon. Wea. Rev.,* **124,** 408–429.

Morton, B. R., 1966: Geophysical vortices. *Prog. Aeronaut. Sci.,* **7,** 145–194.

NOAA, 1990: Morphology of individual thunderstorms and attendant phenomena. *Federal Meteorological Handbook Number 11, Doppler Radar Meteorological Observations: Part B, Doppler Radar Theory and Meteorology,* 207 pp. [Available from Office of the Federal Coordinator for Meteorological Services and Supporting Research, Silver Spring, MD 20910-3315.]

Rasmussen, E. N., J. M. Straka, R. P. Davies-Jones, C. A. Doswell III, F. H. Carr, M. D. Eilts, and D. R. MacGorman, 1994: Verification of the Origins of Rotation in Tornadoes Experiment: VORTEX. *Bull. Amer. Meteor. Soc.,* **75,** 995–1006.

Rott, N., 1958: On the viscous core of a line vortex. *Z. Angew. Math. Physik,* **96,** 543–553.

Rotunno, R., 1977: Numerical simulation of a laboratory vortex. *J. Atmos. Sci.,* **34,** 1942–1956.

——, 1980: Vorticity dynamics of a convective swirling boundary layer. *J. Fluid Mech.,* **97,** 623–640.

——, 1986: Tornadoes and tornadogenesis. *Mesoscale Meteorology and Forecasting,* P. S. Ray, Ed., Amer. Meteor. Soc., 414–436.

——, and J. B. Klemp, 1982: The influence of the shear-induced pressure gradient on thunderstorm motion. *Mon. Wea. Rev.,* **110,** 136–151.

——, and ——, 1985: On the rotation and propagation of numerically simulated supercell thunderstorms. *J. Atmos. Sci.,* **42,** 271–292.

Schlesinger, R. E., 1980: A three-dimensional numerical model of an isolated thunderstorm. Part II: Dynamics of updraft splitting and mesovortex couplet evolution. *J. Atmos. Sci.,* **37,** 395–420.

Scorer, R. S., 1978: *Environmental Aerodynamics.* Ellis Horwood, 488 pp.

Smith, R. K., and L. M. Leslie, 1978: Tornadogenesis. *Quart. J. Roy. Meteor. Soc.,* **104,** 189–199.

——, and ——, 1979: A numerical study of tornadogenesis in a rotating thunderstorm. *Quart. J. Roy. Meteor. Soc.,* **105,** 107–127.

Snow, J. T., 1982: A review of recent advances in tornado vortex dynamics. *Rev. Geophys. Space Phys.,* **20,** 953–964.

Trapp, R. J., 1994: Numerical simulation of the genesis of tornado-like vortices. Ph.D. dissertation, University of Oklahoma, 198 pp. [Available from School of Meteorology, University of Oklahoma, 100 E. Boyd, Norman, OK 73019.]

——, and B. F. Fiedler, 1995: Tornado-like vortexgenesis in a simplified numerical model. *J. Atmos. Sci.,* **52,** 3757–3778.

——, and E. D. Mitchell, 1995: Characteristics of tornadic vortex signatures detected by WSR-88D radars. Preprints, *27th Conf. on Radar Meteorology,* Vail, CO, Amer. Meteor. Soc., 211–212.

Vasiloff, S. V., 1993: Single-Doppler radar study of a variety of tornado types. *The Tornado: Its Structure, Dynamics, Prediction,*

and Hazards, Geophys. Monogr., No. 79, Amer. Geophys. Union, 223–231

Ward, N. B., 1972: The exploration of certain features of tornado dynamics using a laboratory model. *J. Atmos. Sci.,* **29,** 1194–1204.

Wicker, L. J., and R. B. Wilhelmson, 1995: Simulation and analysis of tornado development and decay within a three-dimensional supercell thunderstorm. *J. Atmos. Sci.,* **52,** 2675–2703.

Wilson, J. W., 1986: Tornadogenesis by nonprecipitation induced wind shear lines. *Mon. Wea. Rev.,* **114,** 270–284.

Wilson, T., and R. Rotunno, 1986: Numerical simulation of a laminar end-wall vortex and boundary layer. *Phys. Fluids,* **29,** 3993–4005.

Wood, V. T., and R. A. Brown, 1992: Effects of radar proximity on single-Doppler velocity signatures of axisymmetric rotation and divergence. *Mon. Wea. Rev.,* **120,** 2798–2807.